ROYAL SOCIETY OPEN SCIENCE

royalsocietypublishing.org/journal/rsos

Research

Cite this article: Zhu Y, Rahman T. 2026 Conformational footprints of agonism: differences of inositol 1,4,5-trisphosphate (IP_3) and adenophostin A (AdA) on IP_3 receptor's N-terminal dynamics. *R. Soc. Open Sci.* **13**: 251438. https://doi.org/10.1098/rsos.251438

Received: 5 August 2025
Accepted: 9 January 2026

Subject Category:
Biochemistry, cellular and molecular biology

Subject Areas:
biochemistry, biophysics, computational biology

Keywords:
IP_3 receptor, IP_3, adenophostin A, molecular dynamics, ligand recognition

Author for correspondence:
Taufiq Rahman
e-mail: mtur2@cam.ac.uk

Supplementary material is available online at https://doi.org/10.6084/m9.figshare.c.8249996.

THE ROYAL SOCIETY PUBLISHING

Conformational footprints of agonism: differences of inositol 1,4,5-trisphosphate (IP_3) and adenophostin A (AdA) on IP_3 receptor's N-terminal dynamics

Yu Zhu and Taufiq Rahman

Department of Pharmacology, University of Cambridge, Cambridge, UK

YZ, 0000-0003-1521-1372; TR, 0000-0003-3830-5160

Inositol 1,4,5-trisphosphate receptor (IP_3R) represents a major family of intracellular Ca^{2+}-release channels. Distal to its pore-forming region lies its cytoplasmic N-terminus (NT) that harbours the agonist-binding pocket. Although inositol 1,4,5-trisphosphate (IP_3) is the endogenous agonist, the fungal metabolite adenophostin A (AdA) is known to function as a 'super-agonist', displaying roughly 10-fold higher affinity on binding. Using all-atom molecular dynamics simulations of rat IP_3R1 NT in apo, IP_3-bound and AdA-bound states, we here show that both agonists alter NT's flexibility, yet principal component analysis reveals that AdA drives the domain into broader and distinct conformational substates that are visited by neither the apo nor the IP_3-bound form. AdA occupies a more spacious, hydrophobic pocket, engaging a wider spectrum of transient polar and non-polar contacts and favouring an entropy-dominated binding mode despite fewer enduring hydrogen bonds. Dynamic cross-correlation analysis further demonstrates that AdA enhances long-range correlated motions across the NT domain. Taken together, the data indicate that AdA's superior potency arises from its unique capacity to remodel NT dynamics more profoundly than IP_3, thereby pre-configuring or priming IP_3R for activation gating. These findings refine current models of ligand efficacy and offer a framework for the rational design of next-generation IP_3R modulators.

1. Introduction

Inositol-1,4,5-trisphosphate receptor (IP_3R) functions as a major intracellular calcium-release channel family expressed mainly within the membrane of the endoplasmic reticulum (ER) [1–4]. Structurally akin to the ryanodine receptors, a functional IP_3R is a homo- or hetero-tetramer of subunits [2,5], each of which comprises an N-terminal (NT) agonist-binding region, intermediary regulatory domain and C-terminal transmembrane domains forming the pore [2]. The NT region of the cytosolic assembly, encompassing the suppressor domain (SD; residues 1–224) and bipartite IP_3-binding core (IBC-β: 225–436; IBC-α: 437–604) [3,6], serves as the minimal regulatory unit that transduces agonist engagement into allosteric conformational changes that ultimately result in the pore opening. Three mammalian IP_3R isoforms are known (IP_3R1–3) that differ in tissue distribution and some aspects of regulations [7,8].

The endogenous ligand - inositol 1,4,5-trisphosphate (IP_3) binds within a composite pocket formed at the SD–IBC interface [8]. This interaction, while necessary for activation, is modulated by co-agonists such as Ca^{2+} and ATP, which bind to adjacent regulatory sites and fine-tune the channel's open probability [3,8]. In contrast to IP_3, the fungal metabolite adenophostin A (AdA) demonstrates significantly higher potency. Despite binding to the same pocket, AdA elicits Ca^{2+} release at concentrations approximately 100-fold lower than IP_3, earning it the designation of a 'super-agonist' across all IP_3R isoforms [9]. Thermodynamic analyses of isolated NT fragments attribute this heightened efficacy to a combination of reduced entropic cost upon binding and the ability of AdA, resulting in 10-fold greater affinity compared with IP_3 [10].

In this study, we primarily focused on IP_3R1 given the availability of its structure in apo form or bound with either IP_3 or AdA, unlike the other two isoforms. IP_3R1 predominates in the mammalian brain, with enriched expression in cerebellar Purkinje cells and hippocampal pyramidal neurons, where it orchestrates local and global Ca^{2+} signals implicated in synaptic plasticity, hormone secretion and apoptotic cascades [7]. Aberrant IP_3R1 activity due to some channelopathy mutations has been implicated in several human pathologies that notably include inherited spinocerebellar ataxias (SCA15 and SCA29) and sporadic forms of infantile-onset cerebellar ataxia [11]. Mutations in the *ITPR1* gene, whether through haploinsufficiency or gain-of-function variants [6], have been shown to perturb neuronal Ca^{2+} dynamics and trigger progressive neurodegenerative phenotypes [6,12]. Mechanistic insights from these disorders underscore the need to understand how different ligands influence the conformational landscape and functional output of IP_3R1, particularly within its NT regulatory module.

High-resolution cryo-electron microscopy (cryo-EM) structures have captured full-length rat IP_3R1 in apo, IP_3/Ca^{2+}-bound and AdA/Ca^{2+}-bound conformations at atomic resolution (figure 1A) [14]. These static reconstructions reveal that ligand binding induces coordinated domain rotations, particularly involving the SD and ARM2 domains, with downstream effects transmitted to the pore via helical linkers [7,14]. Although these structural snapshots provide important insights into ligand-bound states, they could not capture the dynamic conformational fluctuations occurring on timescales from picoseconds (ps) to milliseconds (ms) that are critical for channel gating. This could be especially relevant for AdA, which, besides possessing significantly higher affinity for IP_3Rs than IP_3, seems to impart differential kinetics at the single channel level [15], and this differential gating may also underlie the spatio-temporarily distinct Ca^{2+} signals AdA has been shown to generate [16,17]. The mechanistic, especially structural, basis for such distinct efficacy of AdA remains hitherto elusive.

Preliminary molecular dynamics (MD) simulations of the IP_3R1 NT domain have suggested that ligand binding influences IBC hinge dynamics and interdomain communication, yet these studies were constrained by limited simulation time and lacked rigorous energetic evaluation [18]. A detailed, time-resolved characterization of how different ligands sculpt the conformational ensemble of the NT region is essential for understanding agonist efficacy at a mechanistic level. Given the obvious structural differences between the two agonists (figure 1B) and their precise nature of contacts with the NT, we hypothesize that they are likely to influence the dynamics of the NT differently. To address this, the present study applies all-atom MD simulations, combined with principal component analysis (PCA), free-energy landscape reconstruction and binding energy estimation, to compare the conformational dynamics of the rat IP_3R1 NT domain (will be designated as rIP_3R1-NT from now on) in its apo state and upon binding IP_3 or AdA. This integrative approach aims to uncover how a high-affinity agonist like AdA modulates the dynamic behaviour of the NT region relative to IP_3,

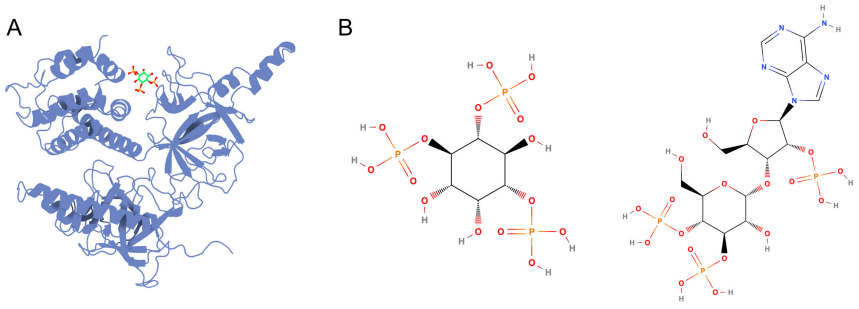

Figure 1. Schematic representation of the rat IP_3R1 NT domain organization and associated ligand molecules. (A) The NT of rat IP_3R1 (shown as blue cartoon representation, from PDB: 8EAR) containing the IP_3 (shown as stick representation) binding core. (B) Two-dimensional representations of the chemical structure of IP_3 and AdA. The three-dimensional structure was rendered using Protein Imager [13].

thereby illuminating the structural and energetic basis of differential ligand efficacy and informing rational design strategies for subtype-selective IP_3R modulators.

2. Results and discussion

2.1. Ligand-induced global dynamics of the rat IP_3R1 N-terminal domain

Ligand binding to the rIP_3R1-NT domain significantly modulates its intrinsic global dynamics. Analysis of backbone root mean square deviation (RMSD) trajectories reveals that the IP_3-bound complex closely mirrors the apo ensemble, with both systems undergoing rapid equilibration and maintaining consistent fluctuations near 4 Å throughout the 500 ns production phase (figure 2A). This similarity suggests that IP_3 binding preserves the intrinsic conformational integrity of the NT domain, exerting minimal perturbation on its native dynamic regime. Conversely, the AdA-bound complex displays notable structural instability, characterized by substantial deviations during the initial phase of the simulation. The RMSD continues to increase for approximately 150 ns before reaching a plateau near 10 Å, indicative of extensive conformational rearrangements and sampling of a markedly distinct and more heterogeneous structural ensemble relative to both the apo and IP_3-bound states.

This ligand-dependent redistribution of flexibility is further resolved by residue-wise root mean square fluctuation (RMSF) profiles (figure 2B). In general, the AdA-bound ensemble exhibits substantially elevated fluctuations relative to both the apo and IP_3-bound states, indicative of a more dynamic and conformationally heterogeneous architecture within the NT domain. Despite this overall increase in flexibility, certain regions display a consistent trend of stabilization upon ligand engagement. Specifically, residues 76–90 and 270–280, corresponding to solvent-exposed loop elements, show diminished amplitudes of motions in both ligand-bound trajectories when compared with the apo state, suggesting a ligand-induced local rigidification of these otherwise flexible segments. Meanwhile, residues 320–350, which constitute a structurally integral portion of the inter-lobe interface, reveal a distinct ligand-specific response. The AdA-bound complex displays a pronounced increase in RMSF values within this region, whereas the apo and IP_3-bound ensembles exhibit comparably subdued fluctuations, implying that AdA binding enhances local flexibility at a site otherwise stabilized in the presence of IP_3. A similar divergence is observed across residues 500–510, forming part of the composite ligand-binding pocket. Here, the AdA-bound state displays elevated mobility relative to the apo form, while IP_3 binding induces a marked suppression of fluctuations, consistent with tighter conformational constraint and more extensive side-chain anchoring within the binding interface. Finally, residues 560–570 display enhanced flexibility in both the AdA-bound and apo trajectories, whereas the IP_3-bound form remains comparatively rigid in this distal loop region. Collectively, these observations delineate a clear dichotomy in ligand-specific dynamic behaviour, whereby IP_3 promotes conformational stabilization of key structural motifs, while AdA induces broader flexibility and redistribution of motion across the NT domain.

Global compaction and solvent exposure analyses, assessed through the radius of gyration (Rg) and solvent-accessible surface area (SASA) profiles, highlight distinct ligand-dependent influences on the structural organization of the rIP_3R1-NT domain (figure 2C,D). Across all simulations, the systems

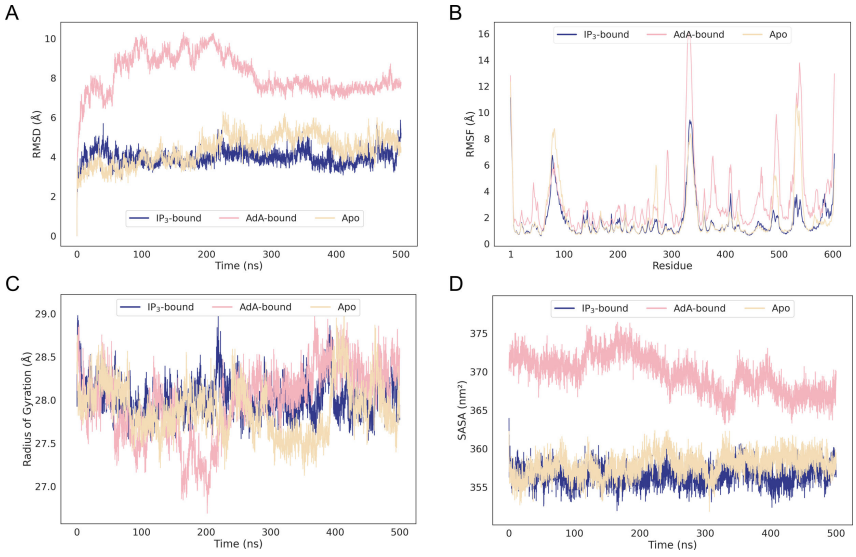

Figure 2. Ligand-induced alterations in rIP$_3$R1-NT dynamics revealed by molecular dynamics simulations. The four panels characterize the conformational space sampled by apo, IP$_3$-bound and AdA-bound rIP$_3$R1-NT. (A) RMSD relative to the initial structure, indicating convergence and overall deviation. (B) Root mean square fluctuation (RMSF) plot, providing insights into the flexibility of individual residues. (C) Radius of gyration (Rg), a measure of molecular compactness and folding. (D) Solvent-accessible surface area (SASA), reflecting changes in the exposed surface area of the molecule. A single representative trajectory is presented for each system (apo: run 2; IP$_3$-bound: run 3; AdA-bound: run 1), while the corresponding results for the remaining independent replicates are provided in the electronic supplementary material.

retain overall structural integrity without evidence of unfolding, yet differ markedly in their degree of compactness. The IP$_3$-bound ensemble remains the most compact, with Rg values consistently centred around 27.8 Å, indicative of a tightly folded and conformationally restrained state. The apo system exhibits slightly broader fluctuations near 28.0 Å, while the AdA-bound complex displays the largest expansion, with transient increases above 28.5 Å, consistent with enhanced global flexibility. This trend is corroborated by the SASA analysis, which reveals the lowest solvent exposure for the IP$_3$-bound ensemble (approx. 356 nm^2), a modest increase for the apo state (approx. 358 nm^2) and a substantially higher value for the AdA-bound form (approx. 372 nm^2). The distinct elevation in solvent-accessible area in the AdA system probably reflects the steric and dynamic influence of its bulky glycopyranosyl tail, which may induce local rearrangements and partial loosening of interdomain contacts to accommodate its extended geometry. All the evidence indicates that IP$_3$ binding promotes structural consolidation and rigidity within the NT domain, whereas AdA binding, facilitated by its glycopyranosyl extension, engenders a more open and conformationally flexible architecture. Detailed analyses of RMSD, RMSF, Rg and SASA for each simulation are presented in electronic supplementary material, figures S1 and S2.

Dynamic cross-correlation maps (DCCMs) were constructed to illustrate the intricate network of correlated motions within the NT domain, revealing three coherent dynamical blocks corresponding to the SD, IBC-β and IBC-α lobes (figure 3A,B). Domain-resolved analyses of the NT architecture point out ligand-specific reorganization across the SD and the two lobes of the IBC-β and IBC-α (figure 3A,B). Relative to both the apo and IP$_3$-bound ensembles, AdA binding is associated with the loosening of SD-IBC coupling, consistent with the expanded Rg and elevated SASA observed for this system. By contrast, IP$_3$ binding preserves a more compact interlobe arrangement with tighter SD engagement, indicative of a stabilized latch-like configuration that restrains interdomain mobility. The apo state occupies an intermediate regime, displaying modest interlobe breathing motions without the separation evident for AdA. Taken together, these domain-level features support a model in which IP$_3$ consolidates SD–IBC contacts and maintains a closed IBC-β/IBC-α juxtaposition, whereas AdA permits greater interdomain plasticity and increased exposure of interfacial surfaces, probably reflecting accommodation of its extended substituents within the pocket. DCCM differences can be referred to electronic supplementary material, figure S3.

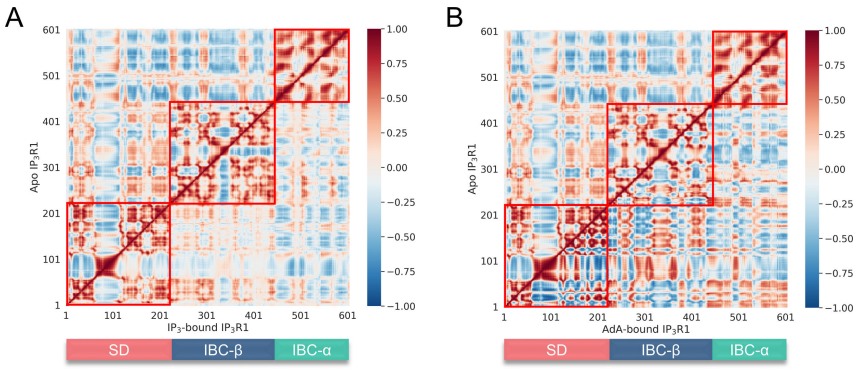

Figure 3. Ligand-induced modulation of IP_3R1 NT dynamics via DCCM. (A) Merged DCCM of apo and IP_3-bound states. (B) Merged DCCM of apo and AdA-bound states. Colour scales represent correlation coefficients from −1 (anti-correlated) to +1 (correlated).

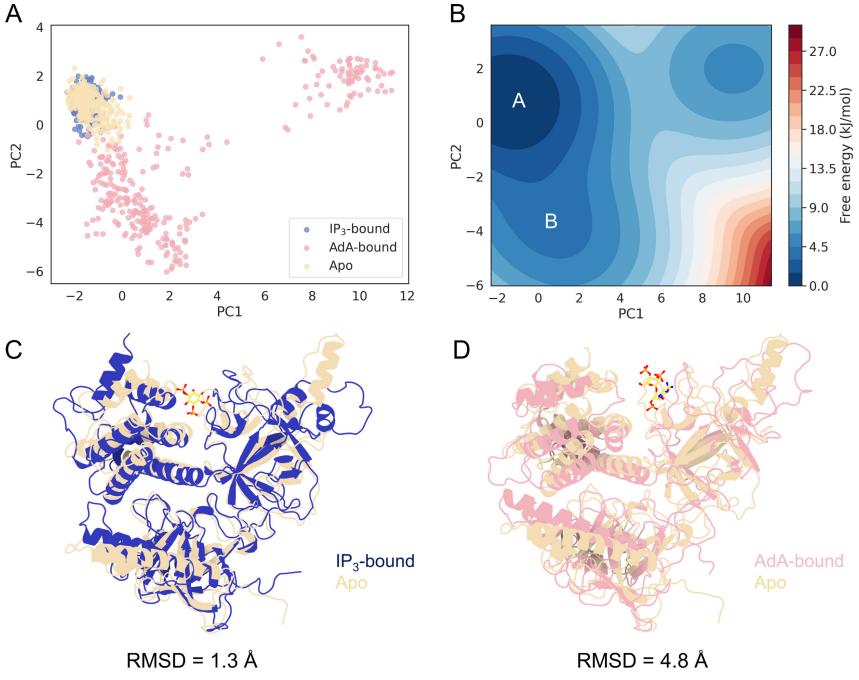

Figure 4. PCA ensemble of conformational states. (A) Two-dimensional projection of PCA ensembles, revealing the major modes of motion and highlighting distinct clusters for the apo, IP_3-bound and AdA-bound states. (B) Pseudo-free energy surface derived from these projections, identifying stable conformational basins and their relative stabilities, with the two major energy basins labelled A and B. (C) Superimposition of representative apo and IP_3-bound conformations sampled from basin A. (D) Superimposition of representative apo and AdA-bound conformations sampled from basin A and B. RMSD values are indicated for each alignment.

2.2. Principal component analysis delineates ligand-specific conformational plasticity

PCA was employed to uncover the major global motions and conformational landscapes sampled by the rIP_3R1-NT under various ligand-bound states. To capture the full spectrum of conformational variability, the simulated ensembles of the apo, IP_3-bound and AdA-bound NT domains were concatenated. Projection of the conformational ensembles onto the two most dominant principal components, PC1 and PC2 (figure 4A), which collectively highlight the maximal amplitudes of backbone atomic motions, enabled the derivation of a two-dimensional pseudo-free energy landscape (figure 4B). This landscape serves to elucidate the predominant global conformational dynamics of the NT domain.

Analysis of the pseudo-free energy landscape, derived from projections onto the PC1–PC2 plane, revealed distinct clustering behaviours corresponding to different ligand states. Notably, the conformational ensembles of the apo and IP_3-bound NT domains exhibited substantial overlap, indicating a high degree of conformational similarity and shared accessible conformational space. This suggests that while IP_3 binding induces specific interactions, the overall global dynamics and accessible

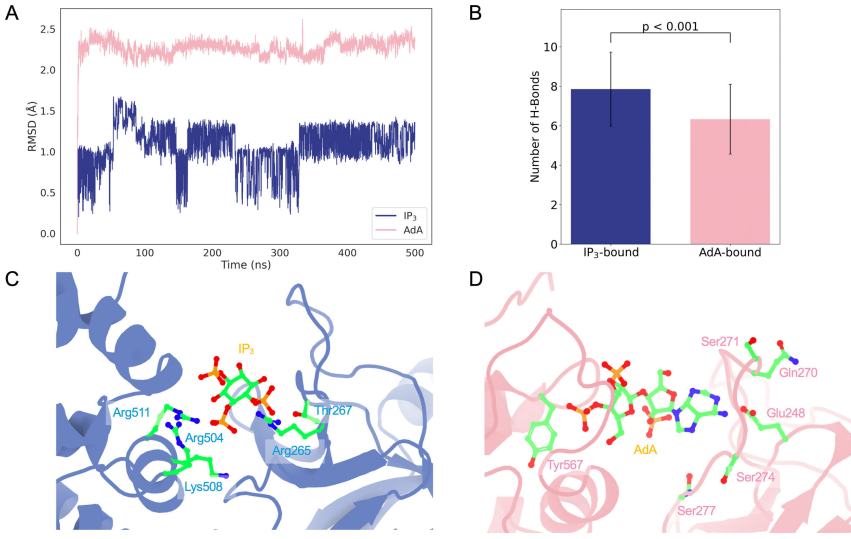

Figure 5. Ligand dynamics and hydrogen bonding in IP_3 and AdA binding. (A) ligand root mean square deviation (RMSD) for IP_3 and AdA during simulations. The results presented derive from a representative trajectory for each holo system (IP_3-bound: run 3; AdA-bound: run 1), whereas the results obtained from the remaining independent replicates are reported in the electronic supplementary material. (B) Number of hydrogen bonds formed over simulation time. Histograms representing average number of hydrogen bonds (as mean ± s.d.) for IP_3- and AdA-bound systems obtained from three independent simulation runs. Statistical comparison was performed using unpaired Student's *t*-test. (C) and (D) depict the binding of IP_3 and AdA to the rIP_3R1-NT.

conformational states of the NT domain remain largely similar to the apo state, with relatively subtle changes in backbone dynamics. In stark contrast, the AdA-bound NT domain occupied a clearly separated and distinct region within the PC1–PC2 conformational space. This pronounced spatial separation strongly implies that AdA binding induces significantly different conformational reconfigurations, driving the NT into a substantially different state and exploring regions of the conformational landscape not readily accessible in either the apo or IP_3-bound forms.

Random conformations sampled from the lowest energy basins within the pseudo-free energy landscape further corroborated these findings. The AdA-bound conformations showed a significant structural divergence from those of the apo and IP_3-bound basins (figure 4C,D). This observation is in direct alignment with DCCM analysis, which previously indicated greater alterations in residue–residue correlations upon AdA binding compared with IP_3 binding. The convergence of PCA and DCCM outputs robustly strengthens the conclusion that AdA binding induces more extensive and differential conformational changes within the NT compared with IP_3 binding. This differential effect on NT dynamics provides a potential mechanistic basis for AdA's reported greater agonist potency and higher affinity.

2.3. Dynamic dissimilarities and pocket features: unravelling ligand binding modes of IP_3 and AdA

Ligand RMSD revealed distinct binding stabilities and conformational behaviours within the NT domain pocket (figure 5A). Following a brief equilibration phase, IP_3 rapidly adopts a highly stable orientation, maintaining tightly clustered fluctuations around a mean RMSD of approximately 1.0 Å throughout the 500 ns production simulation. This restrained dynamic profile indicates a well-defined and rigid binding pose, consistent with strong anchoring interactions between the phosphate groups and the surrounding basic residues of the binding cleft. In contrast, AdA exhibits persistently higher RMSD values, stabilizing early in the simulation at approximately 2.3 Å and maintaining this broader fluctuation envelope over the full trajectory. The elevated RMSD and reduced temporal variability suggest a stable yet more conformationally tolerant binding mode, characterized by minor reorientations and micro-adjustments within the pocket rather than large-scale displacement. This enhanced flexibility probably originates from AdA's additional ribose and glycopyranosyl extensions, which introduce additional steric bulk and hydrogen-bonding capacity, permitting the ligand to modulate its local conformation while preserving key anchoring contacts. Such adaptive plasticity may enable

AdA to maintain stable binding across subtly different microenvironments within the pocket, thereby supporting its high-affinity and super-agonistic behaviour observed experimentally.

Comparative analysis of ligand-receptor hydrogen bonding profiles revealed distinct interaction patterns for IP_3 and AdA within the NT domain (figure 5B). Quantitatively, IP_3 maintained a significantly higher number of hydrogen bonds, averaging approximately eight persistent interactions across the production trajectories, in contrast to the AdA-bound complex, which exhibited a reduced mean of around six hydrogen bonds (Student's *t*-test; $p < 0.001$). The IP_3-associated network was dominated by anchoring residues, including Arg504, Lys508 and Arg511, which together stabilize the phosphate moieties through the canonical tripartite electrostatic clamp. Additional contributions from Arg265 and Thr267 further reinforced the ligand's positional restraint within the binding cleft. This dense and persistent hydrogen-bonding pattern is indicative of a highly specific, enthalpy-driven binding mode that rigidifies the IP_3-NT complex and restricts local flexibility. In distinction, the AdA-bound ensemble exhibited a smaller but more spatially dispersed set of hydrogen bond interactions, engaging residues such as Glu248, Gln270, Ser271, Ser274, Ser277 and the distal Tyr567. The lower number yet broader distribution of these contacts reflects a more delocalized interaction network, consistent with AdA's extended chemical architecture. The presence of its additional ribose and glycopyranosyl substituents probably introduces steric and conformational plasticity that permits transient hydrogen-bond exchange and reorientation within the pocket. This behaviour suggests that AdA's superior binding affinity and super-agonistic efficacy arise not from an increased number of classical hydrogen bonds but rather from an optimized balance between local adaptability, van der Waals complementarity and entropic stabilization within the broader NT interface.

Pocket analysis revealed both shared and distinct contributions to the ligand binding pockets of IP_3 and AdA. While the IP_3 binding pocket was characterized by interactions with Arg265, Thr267, Gly268, Arg269, Ala275, Arg504, Lys508, Arg511, Tyr567, Arg568 and Lys569, the AdA binding pocket exhibited a more expansive set of residues. A significant overlap of nine residues (Thr267, Gly268, Arg269, Ala275, Arg504, Lys508, Tyr567, Arg568 and Lys569) was observed between the two binding sites, underscoring common determinants of recognition. However, the AdA binding interface was notably larger, expanding upon the canonical IP_3 pocket with 12 additional residues. This expansion resulted in a dramatic increase in pocket volume, from a mean of 335.8 $Å^3$ for the IP_3-bound state to 660.4 $Å^3$ for the AdA-bound complex, accompanied by a significantly higher hydrophobic score for AdA (Student's *t*-test; $p < 0.001$). This expanded pocket, coupled with enhanced hydrophobic contributions, is particularly significant given the polar nature of the NT binding site. Consistent with these quantitative pocket descriptors, time-resolved snapshots show a more deformable, accommodating cavity in the AdA-bound ensemble (figure 6). The ability of AdA to leverage a broader interaction surface, incorporating both polar and non-polar contacts, may account for its superior affinity and agonist efficacy, as it allows for a more finely tuned recognition mechanism that can compensate for fewer direct hydrogen bonds. The increased ligand RMSD observed for AdA might therefore reflect an optimal dynamic state that facilitates a more comprehensive engagement with its larger, more diverse binding pocket, ultimately translating to a greater functional effect on receptor activation.

2.4. Energetic determinants of ligand binding to the rIP$_3$R1 NT

Triplicate 500 ns trajectories of the IP_3-bound and AdA-bound rIP$_3$R1-NT were subjected to analysis via the molecular mechanics/Poisson–Boltzmann surface area (MM/PBSA) protocol. The analysis further clarified the energetic basis of ligand recognition within the NT domain, revealing distinct thermodynamic signatures consistent with the structural and dynamical observations (electronic supplementary material, table S1). The IP_3-bound complex displayed a substantially more favourable enthalpic contribution (ΔH = −156.2 kcal mol^{-1}), arising from strong electrostatic and hydrogen-bonding interactions that stabilize its compact, phosphate-anchored binding mode. This enthalpic dominance aligns with the RMSD and hydrogen-bond analyses, which showed that IP_3 maintains a highly ordered and rigid pose supported by a dense polar interaction network. By comparison, AdA binding was characterized by a weaker enthalpic stabilization (ΔH = −92.2 kcal mol^{-1}) but a markedly larger entropic contribution ($-T\Delta S$ = 150.4 kcal mol^{-1}), reflecting the enhanced conformational flexibility observed in the MD trajectories. Energy decomposition indicated that AdA engages a broader binding interface incorporating both transient polar and hydrophobic contacts, consistent with the elevated RMSD, reduced number of hydrogen bonds and greater solvent exposure seen in the SASA and Rg analyses. The substantial entropic term is probably driven by the mobility of AdA's glycopyranosyl and ribose extensions, which allow local reorientation and dynamic redistribution of contacts

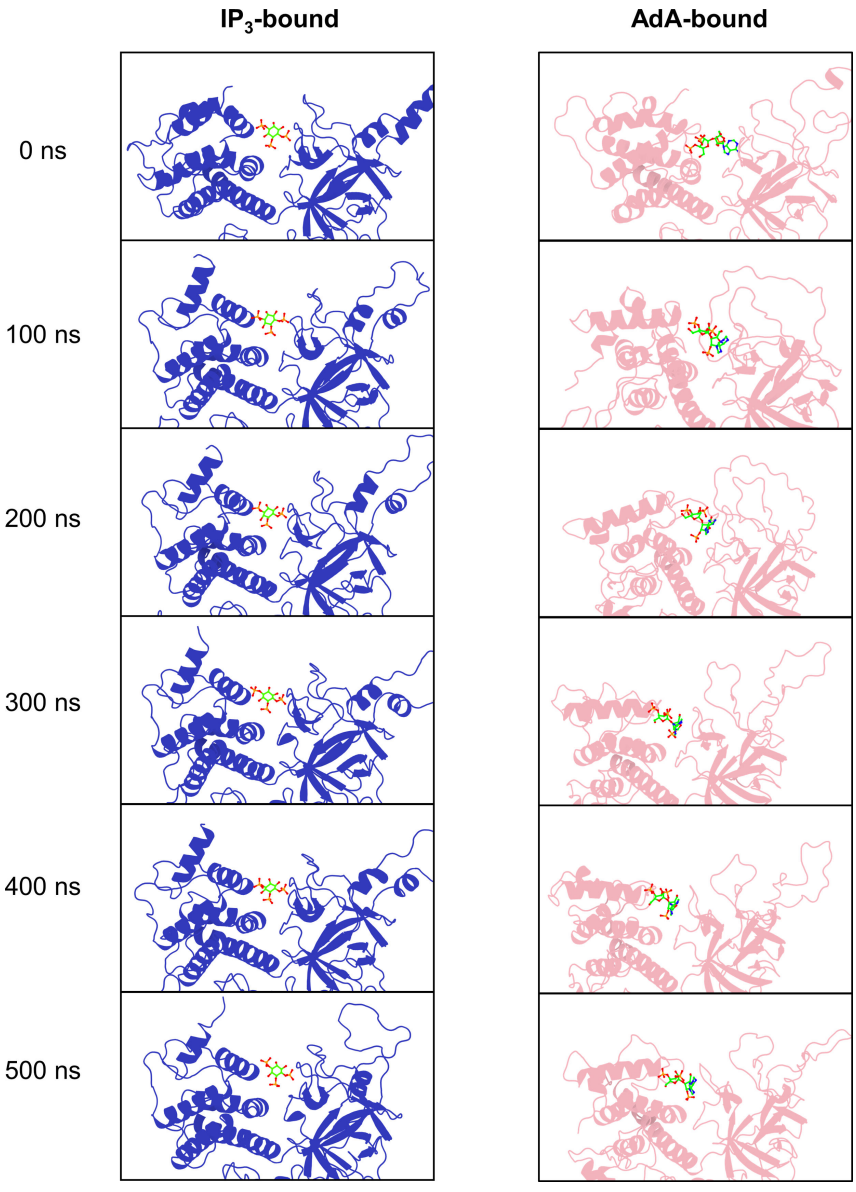

Figure 6. Characterization of binding pocket properties in IP_3- and AdA-bound rIP_3R1-NT systems. Conformational dynamics of the ligand binding pocket within the rIP_3R1-NT. Snapshots captured at 100 ns intervals illustrate the dynamic nature of the binding pocket in both IP_3- and AdA-bound states.

within the pocket while maintaining overall binding stability. Although the absolute magnitudes of the interaction-entropy components warrant cautious interpretation, the observed trends are fully consistent with the domain-level dynamics. IP_3 binding is predominantly enthalpy-driven, reflecting the strong electrostatic and hydrogen-bonding network that enforces a compact and conformationally restrained binding mode. By comparison, AdA binding is characterized by a greater entropic contribution, supported by hydrophobic complementarity and enhanced conformational plasticity. This hydrophobic component facilitates an entropy-modulated, dynamically adaptable binding mode, consistent with the structural evidence of loosened SD-IBC coupling, increased interdomain flexibility and expanded solvent exposure. In general, these findings depict two energetically distinct but functionally convergent recognition strategies: the binding of the IP_3 stabilizes the NT domain through electrostatic consolidation and conformational rigidity, whereas AdA achieves high-affinity engagement via flexible, entropy-compensated adaptation of an expanded interaction interface.

Given the limitations encountered with MM/PBSA, an alternative approach to binding affinity prediction was employed using Boltz-2 [19], a method recognized for its comparable accuracy to free energy perturbation (FEP). The Boltz-2 scores demonstrably supported the experimental observations, with IP_3 yielding a score of –0.063 and AdA achieving a score of –0.298, where lower scores signify

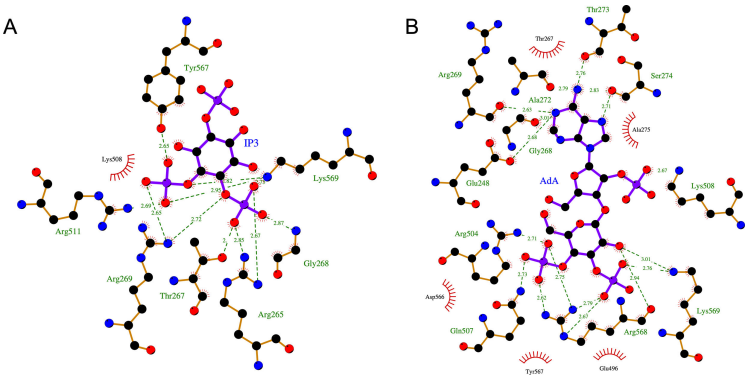

Figure 7. Two-dimensional ligand interaction diagrams for two IP_3R agonists. (A) Binding mode of IP_3 with the IP_3R1-NT. (B) Binding mode of AdA with the IP_3R1-NT. Hydrogen bonds are shown as green dashed lines connecting the donor and acceptor atoms, with distances indicated in Å. Hydrophobic interactions are represented by red spoked arcs that emanate from the atoms involved in contact, illustrating the close van der Waals proximity between the ligand and specific non-ligand atoms. The figures were generated using LigPlot+ [20].

enhanced binding affinity. Consequently, AdA demonstrated superior binding affinity, in accordance with experimental data. Atomic-level interaction analysis, derived from the Boltz-2 modelling results and depicted in figure 7, confirmed a greater prevalence of hydrophobic interactions for AdA. Detailed prediction results can be found in electronic supplementary material, table S3.

Synthesizing the energetic and decomposition analyses, crucial insights into the distinct binding mechanisms and functional implications for the IP_3R emerge from the observed differences in hydrogen bonding patterns between IP_3 and AdA. The consistent formation of numerous stable hydrogen bonds by IP_3 with key residues within the NT domain aligns with established models of IP_3R activation. This extensive and specific hydrogen bond network suggests that IP_3 binding is predominantly enthalpy-driven, resulting in a highly constrained and rigid interaction within the ligand-binding pocket. Such a constrained binding mode is characteristic of a direct agonist, where precise positioning and robust anchoring of the ligand are essential for initiating the conformational changes required for channel opening.

By comparison, AdA, despite exhibiting a higher affinity, forms fewer persistent hydrogen bonds, with these interactions distributed across a broader set of residues. This indicates that AdA's binding is not solely reliant on a limited number of strong, classical hydrogen bonds but probably incorporates a more diverse array of interactions, including weaker, non-classical hydrogen bonds, van der Waals forces and hydrophobic contacts. The redistribution of contacts observed for AdA, potentially compensating for reduced per-bond lifetime, points towards a more entropy-balanced binding mode. This implies that while individual hydrogen bonds may be less persistent, the overall binding energy is maintained or enhanced by a greater degree of conformational flexibility or solvent displacement, leading to a favourable entropic contribution. The larger entropic gain associated with AdA binding relative to IP_3 binding is also consistent with AdA's larger apolar surface, which would induce a greater entropy gain from ligand desolvation and hydrophobic interactions during binding. Therefore, the binding of AdA is predominantly driven by these varied interactions.

Collectively, these results describe a ligand-specific balance between rigidity and adaptability in binding. IP_3 secures a tightly constrained, hydrogen-bond-rich configuration within a compact, highly polar pocket, reflecting its enthalpy-driven stabilization through extensive electrostatic interactions and substantial desolvation. Alternatively, AdA engages a more spacious and hydrophobic cavity, forming fewer persistent hydrogen bonds but maintaining stability through transient polar contacts. This interaction pattern is accompanied by a lower desolvation penalty and a larger entropic contribution, consistent with an entropy-favoured, dynamically modulated binding mode. Such intrinsic plasticity probably underlies AdA's high-affinity, super-agonistic behaviour, enabling the NT clamp to sample conformations that more effectively transmit ligand-induced structural changes to the downstream gating machinery.

The present findings also provided a mechanistic foundation for guiding the rational design of potent IP_3R modulators. By integrating conformational dynamics, residue-level flexibility and thermodynamic profiles, this work highlights the importance of both local and global structural adaptability in defining ligand efficacy. The simulations reveal that the NT domain does not operate

as a rigid recognition module but instead functions as a dynamic allosteric integrator, capable of transmitting subtle variations in ligand-induced flexibility to distal gating elements. This observation suggests that effective modulators should not merely optimize static binding affinity but also tune the conformational ensemble of the NT domain to favour either activation or inhibition. In practical terms, ligands that simultaneously balance strong anchoring interactions within the binding pocket with controlled flexibility at peripheral sites may best exploit the receptor's intrinsic allosteric plasticity. Furthermore, the combined use of MD and free energy analyses demonstrated here provides a robust computational framework for predicting how candidate compounds reshape domain coupling, solvent exposure and entropic contributions. Such multi-scale insights can inform structure-based screening and lead optimization, facilitating the identification of molecules that precisely modulate IP_3R activity with improved potency and selectivity, offering a promising route for developing potent and selective IP_3R modulators.

3. Material and methods

3.1. System preparation

Three simulation systems representing the NT region (residues 1–604) of rat type 1 inositol 1,4,5-trisphosphate receptor (IP_3R1; UniProt: P29994) were prepared: apo (ligand-free), IP_3-bound [14] and AdA-bound systems [21]. The IP_3-bound model was derived from the cryo-EM structure of rat IP_3R1 complexed with IP_3 (PDB: 8EAR) [21], from which the relevant residues and ligand were extracted; unresolved regions (residues 1–5 and 323–349) were reconstructed using Modeller v. 10.4 [22], guided by the full-length UniProt sequence (https://www.uniprot.org/uniprotkb/P29994/entry). The apo system was generated by removing the IP_3 ligand from the IP_3-bound structure without introducing additional modifications, thereby ensuring structural consistency across systems. The AdA-bound system was constructed using the corresponding cryo-EM structure (PDB: 6MU1), with residues 1–604 and the AdA ligand extracted and missing segments (residues 1–3, 322–352, 533–545 and 586–595) similarly modelled using Modeller v. 10.4 [22]. All structures were subjected to rigorous stereochemical validation and visual inspection to confirm structural integrity.

All three systems underwent preparation via a consistent, previously established protocol using CHARMM-GUI [23]. Protonation states appropriate to pH 7.4 were assigned by PROPKA 3.5, and the terminus was capped with acetyl and N-methylamide groups [24,25]. Ligand topologies and charges were generated using CGenFF within the CHARMM-GUI platform [23,26]. Each receptor (with or without ligand) was submitted to CHARMM-GUI Solution Builder for solvation in a cubic box of TIP3P water extending at least 10 Å from any protein atom [23,27,28]. Systems were neutralized and brought to 0.15 M NaCl with CHARMM ion parameters. Proteins were described with the CHARMM36m force field [29], ions and water with the matching CHARMM parameters, and ligands with the refined CGenFF topologies, ensuring a consistent additive potential across all components.

3.2. Molecular dynamics simulations

Each solvated system was first subjected to positional-restrained energy minimization. Positional restraints of 400 kJ mol^{-1} nm^{-2} on backbone heavy atoms and 40 kJ mol^{-1} nm^{-2} on side-chain heavy atoms were activated through pre-processor macros. The structures were then relaxed for 5000 steps with the steepest-descent integrator. The run was halted once the maximum residual force on any atom fell below 1000 kJ mol^{-1} nm^{-1}.

The structures then passed through the multi-stage position-restrained equilibration workflow: canonical (number–volume–temperature (NVT)) and isothermal-isobaric (number–pressure–temperature (NPT)) ensembles. Production trajectories were propagated with GROMACS 2023.3 across a distributed computing environment [30], including local machines with NVIDIA RTX A4000 graphics processing units (GPUs) and high-performance computing (HPC) cluster powered by NVIDIA A100 GPUs. Molecular motion was integrated with the leap-frog algorithm using a 2 fs time-step, and every covalent bond involving hydrogen was rigidified with the linear constraint solver (LINCS) algorithm set to fourth-order expansion [31]. Electrostatic interactions were treated with the particle-mesh Ewald (PME) method, employing a real-space cut-off of 1.2 nm, a Fourier grid spacing of 0.12 nm and a PME interpolation order of four. Lennard–Jones forces were smoothed to zero between 1.0 and 1.2 nm under the Verlet cut-off scheme [32]. Temperature control at 303.15 K was achieved with a stochastic

velocity-rescale thermostat, coupled separately to the solute and solvent groups with a relaxation time of 1 ps. Pressure was maintained isotropically at 1 bar by the C-rescale barostat, using a coupling constant of 5 ps and an isothermal compressibility of 4.5×10^{-5} bar^{-1}. Linear centre-of-mass motion was removed from the solute and solvent groups every 100 integration steps. For each of the apo, IP_3-bound and AdA-bound systems, three independent production runs of 500 ns were executed, furnishing an aggregate sampling of 4.5 µs. System coordinates were saved every 50 ps in compressed XTC format, while energy terms and thermostat/barostat statistics were recorded at 1 ps intervals, ensuring a high-resolution dataset for subsequent structural, dynamical and energetic analyses.

3.3. Trajectory analysis

Initial processing of all raw MD trajectories was performed with GROMACS 2023.3 for the removal of periodic boundary conditions [30]. Subsequent analysis of structural stability and flexibility canonical metrics was achieved via an in-house Python script integrating MDAnalysis and MDTraj [33,34]. These metrics included RMSD relative to the initial cryo-EM model, per-residue RMSF, radius of gyration and SASA. Values were extracted per replica and averaged across the three independent replicates.

Conformational landscapes were elucidated through PCA of the weighted covariance matrix of Cα Cartesian coordinates. A pseudo-free energy surface, reconstructed via Boltzmann inversion of the two-dimensional population histogram, served to define metastable basins. Long-range correlated motions were quantitatively assessed from the same atomic displacements by the dynamic cross-correlation matrix (DCCM), as implemented in Bio3D [35], with coupled motions visualized on a blue-to-red scale.

Atomic-resolution characterization of protein–ligand recognition included the calculation of hydrogen-bond occupancies between IP_3 or AdA and protein side chains. This was performed using the HBonds plug-in of VMD 1.9.3 [36], applying stringent geometric criteria of a 3 Å donor-acceptor distance and a 20° donor-hydrogen-acceptor angle. Representative structures were rendered for visualization using VMD 1.9.3 [36] and Protein Imager [13]. Protein–ligand interaction profiles, specifically encompassing hydrogen bonds, π–π stacking, cation-π contacts, salt bridges, water bridges and hydrophobic contacts, were derived from selected conformational snapshots. This analysis was performed using the standalone LigPlot+ v. 2.2.9 [20].

To quantify how ligand binding remodels the interior cavity, the pre-processed trajectories were examined with mdpocket in dynamic mode. The ligand binding pocket was evaluated across 1500 evenly spaced snapshots for each holo system to derive temporal maps of pocket volume, depth, hydrophobicity and polarity. Time series were smoothed with a 1 ns moving average for comparison between IP_3- and AdA-bound ensembles.

3.4. Binding energy assessment

Binding energetics were evaluated using the MM/PBSA workflow implemented in gmx_MMPBSA 1.6.4 [37,38]. Five hundred frames per replication were uniformly sampled from the final 50 ns of the equilibrated production trajectory and were analysed at a temperature of 303.15 K, consistent with the molecular dynamics simulations. Molecular mechanics energies were calculated using the CHARMM36m force field [29]. Polar solvation energies were determined using a finite-difference Poisson–Boltzmann solver, with an ionic strength of 0.15 M and employing the CHARMM PB-radii set. Non-polar solvation contributions were estimated via the SASA method. Further analyses included the application of an interaction entropy (IE) correction and a per-residue decomposition for all atoms situated within 4.5 Å of the ligand. IE calculations were performed using the final stage frames of each trajectory. Because the standard deviation of the interaction energies exceeded 3.6 kcal mol^{-1}, the resulting $-T\Delta S$ estimates are interpreted qualitatively, as indicators of relative entropic trends rather than absolute thermodynamic quantities.

In parallel with the aforementioned analyses, binding affinities were estimated using the recently released Boltz-2 model [19]. This innovative AI model unifies structure and affinity prediction, achieving accuracies comparable to FEP calculations while demonstrating a computational speed-up exceeding 1000-fold. For each holo system, the Boltz-2 model received the amino acid sequence of rat IP_3R1 NT and the SMILES string of the respective ligand as input. This methodology enabled the precise quantification of the specific affinity for various ligands. The model reports binding affinity values as log (IC_{50}), which are derived from a half-maximal inhibitory concentration (IC_{50}) value

expressed in micromolar (μM) units. Critically, lower log (IC_{50}) values are indicative of a stronger predicted binding affinity.

4. Conclusions

This study used all-atom MD simulations to elucidate the differential effects of IP_3 and AdA on the conformational dynamics of the rIP_3R1-NT. While both agonists modulate NT flexibility relative to the apo state, AdA uniquely promotes substantially broader and distinct conformational substates, as demonstrated by principal component analysis, which reveals that the AdA-bound NT occupies a conformational space not accessed by either the apo or IP_3-bound forms. This deeper conformational perturbation by AdA, coupled with its greater binding affinity, is attributed to its engagement with a more expansive and hydrophobically enriched binding pocket, enabling a broader, more diverse array of polar and non-polar interactions despite forming fewer direct hydrogen bonds. In summary, these findings suggest that AdA more effectively biases the NT towards a primed, activation-prone conformational ensemble, which may facilitate coupling to downstream gating processes and provides mechanistic insight into differential ligand efficacy relevant to the rational design of IP_3R modulators.

Ethics. This work did not require ethical approval from a human subject or animal welfare committee.

Data accessibility. Available on Dryad [39].

Supplementary material is available online [40].

Declaration of AI use. We have not used AI-assisted technologies in creating this article.

Authors' contributions. Y.Z.: formal analysis, investigation, methodology, visualization, writing—original draft; T.R.: conceptualization, resources, supervision, writing—review and editing.

Both authors gave final approval for publication and agreed to be held accountable for the work performed therein.

Conflict of interest declaration. We declare we have no competing interests.

Funding. Y.Z. was supported by the Percy Lander studentship from Downing College.

References

1. Finch EA, Turner TJ, Goldin SM. 1991 Calcium as a coagonist of inositol 1,4,5-trisphosphate-induced calcium release. *Science* **252**, 443–446. (doi:10.1126/science.2017683)
2. Berridge MJ. 2005 Unlocking the secrets of cell signaling. *Annu. Rev. Physiol*. **67**, 1–21. (doi:10.1146/annurev.physiol.67.040103.152647)
3. Prole DL, Taylor CW. 2016 Inositol 1,4,5-trisphosphate receptors and their protein partners as signalling hubs. *J. Physiol.* **594**, 2849–2866. (doi:10.1113/JP271139)
4. Streb H, Irvine RF, Berridge MJ, Schulz I. 1983 Release of Ca^{2+} from a nonmitochondrial intracellular store in pancreatic acinar cells by inositol-1,4,5-trisphosphate. *Nature* **306**, 67–69. (doi:10.1038/306067a0)
5. Yoshikawa F, Morita M, Monkawa T, Michikawa T, Furuichi T, Mikoshiba K. 1996 Mutational analysis of the ligand binding site of the inositol 1,4,5-trisphosphate receptor. *J. Biol. Chem*. **271**, 18277–18284. (doi:10.1074/jbc.271.30.18277)
6. Kerkhofs M, Seitaj B, Ivanova H, Monaco G, Bultynck G, Parys JB. 2018 Pathophysiological consequences of isoform-specific IP_3 receptor mutations. *Biochim. Et Biophys. Acta Mol. Cell Res*. **1865**, 1707–1717. (doi:10.1016/j.bbamcr.2018.06.004)
7. Hamada K, Mikoshiba K. 2020 IP_3 receptor plasticity underlying diverse functions. *Annu. Rev. Physiol*. **82**, 151–176. (doi:10.1146/annurev-physiol-021119-034433)
8. Prole DL, Taylor CW. 2019 Structure and function of IP_3 receptors. *Cold Spring Harb. Perspect. Biol.* **11**, a035063. (doi:10.1101/cshperspect.a035063)
9. Ding Z, Rossi AM, Riley AM, Rahman T, Potter BVL, Taylor CW. 2010 Binding of inositol 1,4,5-trisphosphate (IP_3) and adenophostin A to the N-terminal region of the IP_3 receptor: thermodynamic analysis using fluorescence polarization with a novel IP_3 receptor ligand. *Mol. Pharmacol*. **77**, 995–1004. (doi:10.1124/mol.109.062596)
10. Rossi AM, Riley AM, Tovey SC, Rahman T, Dellis O, Taylor EJA, Veresov VG, Potter BVL, Taylor CW. 2009 Synthetic partial agonists reveal key steps in IP_3 receptor activation. *Nat. Chem. Biol*. **5**, 631–639. (doi:10.1038/nchembio.195)
11. Ando H, Hirose M, Mikoshiba K. 2018 Aberrant IP_3 receptor activities revealed by comprehensive analysis of pathological mutations causing spinocerebellar ataxia 29. *Proc. Natl Acad. Sci. USA* **115**, 12259–12264. (doi:10.1073/pnas.1811129115)
12. Gambardella J, Lombardi A, Morelli MB, Ferrara J, Santulli G. 2020 Inositol 1,4,5-trisphosphate receptors in human disease: a comprehensive update. *J. Clin. Med*. **9**, 1096. (doi:10.3390/jcm9041096)
13. Tomasello G, Armenia I, Molla G. 2020 The protein imager: a full-featured online molecular viewer interface with server-side HQ-rendering capabilities. *Bioinformatics* **36**, 2909–2911. (doi:10.1093/bioinformatics/btaa009)

14. Fan G, Baker MR, Wang Z, Seryshev AB, Ludtke SJ, Baker ML, Serysheva II. 2018 Cryo-EM reveals ligand induced allostery underlying $InsP_3R$ channel gating. *Cell Res*. **28**, 1158–1170. (doi:10.1038/s41422-018-0108-5)
15. Mak DO, McBride S, Foskett JK. 2001 ATP-dependent adenophostin activation of inositol 1,4,5-trisphosphate receptor channel gating: kinetic implications for the durations of calcium puffs in cells. *J. Gen. Physiol*. **117**, 299–314. (doi:10.1085/jgp.117.4.299)
16. Marchant JS, Parker I. 1998 Kinetics of elementary Ca2+ puffs evoked in Xenopus oocytes by different Ins(1,4,5)P3 receptor agonists. *Biochem. J*. **334 (Pt 3)**, 505–509. (doi:10.1042/bj3340505)
17. Bird GS, Takahashi M, Tanzawa K, Putney JW. 1999 Adenophostin A induces spatially restricted calcium signaling in *Xenopus laevis* oocytes. *J. Biol. Chem*. **274**, 20643–20649. (doi:10.1074/jbc.274.29.20643)
18. Moritsugu K, Ito T, Kidera A. 2019 Allosteric response to ligand binding: molecular dynamics study of the N-terminal domains in IP_3 receptor. *Biophys. Physicobiol.* **16**, 232–239. (doi:10.2142/biophysico.16.0_232)
19. Passaro S *et al*. 2025 Boltz-2: towards accurate and efficient binding affinity prediction. *bioRxiv.* 2025.06.14.659707. (doi:10.1101/2025.06.14.659707)
20. Laskowski RA, Swindells MB. 2011 LigPlot+: multiple ligand-protein interaction diagrams for drug discovery. *J. Chem. Inf. Model*. **51**, 2778–2786. (doi:10.1021/ci200227u)
21. Fan G *et al*. 2022 Conformational motions and ligand-binding underlying gating and regulation in IP_3R channel. *Nat. Commun*. **13**, 6942. (doi:10.1038/s41467-022-34574-1)
22. Sali A, Blundell TL. 1993 Comparative protein modelling by satisfaction of spatial restraints. *J. Mol. Biol*. **234**, 779–815. (doi:10.1006/jmbi.1993.1626)
23. Jo S, Kim T, Iyer VG, Im W. 2008 CHARMM-GUI: a web-based graphical user interface for CHARMM. *J. Comput. Chem*. **29**, 1859–1865. (doi:10.1002/jcc.20945)
24. Olsson MHM, Søndergaard CR, Rostkowski M, Jensen JH. 2011 PROPKA3: consistent treatment of internal and surface residues in empirical pKa predictions. *J. Chem. Theory Comput*. **7**, 525–537. (doi:10.1021/ct100578z)
25. Søndergaard CR, Olsson MHM, Rostkowski M, Jensen JH. 2011 Improved treatment of ligands and coupling effects in empirical calculation and rationalization of pKa values. *J. Chem. Theory Comput*. **7**, 2284–2295. (doi:10.1021/ct200133y)
26. Vanommeslaeghe K *et al*. 2010 CHARMM general force field: a force field for drug-like molecules compatible with the CHARMM all-atom additive biological force fields. *J. Comput. Chem*. **31**, 671–690. (doi:10.1002/jcc.21367)
27. Lee J *et al*. 2016 CHARMM-GUI input generator for NAMD, GROMACS, AMBER, OpenMM, and CHARMM/OpenMM simulations using the CHARMM36 additive force field. *J. Chem. Theory Comput*. **12**, 405–413. (doi:10.1021/acs.jctc.5b00935)
28. Jorgensen WL, Chandrasekhar J, Madura JD, Impey RW, Klein ML. 1983 Comparison of simple potential functions for simulating liquid water. *J. Chem. Phys*. **79**, 926–935. (doi:10.1063/1.445869)
29. Huang J, Rauscher S, Nawrocki G, Ran T, Feig M, de Groot BL, Grubmüller H, MacKerell AD. 2017 CHARMM36m: an improved force field for folded and intrinsically disordered proteins. *Nat. Methods* **14**, 71–73. (doi:10.1038/nmeth.4067)
30. Abraham MJ, Murtola T, Schulz R, Páll S, Smith JC, Hess B, Lindahl E. 2015 GROMACS: high performance molecular simulations through multi-level parallelism from laptops to supercomputers. *SoftwareX* **1–2**, 19–25. (doi:10.1016/j.softx.2015.06.001)
31. Hess B, Bekker H, Berendsen HJC, Fraaije JGEM. 1997 LINCS: a linear constraint solver for molecular simulations. *J. Comput. Chem*. **18**, 1463–1472. (doi:10.1002/(sici)1096-987x(199709)18:123.3.co;2-l)
32. Verlet L. 1967 Computer 'experiments' on classical fluids. I. Thermodynamical properties of Lennard-Jones molecules. *Phys. Rev.* **159**, 98–103. (doi:10.1103/PhysRev.159.98)
33. Michaud-Agrawal N, Denning EJ, Woolf TB, Beckstein O. 2011 MDAnalysis: a toolkit for the analysis of molecular dynamics simulations. *J. Comput. Chem*. **32**, 2319–2327. (doi:10.1002/jcc.21787)
34. McGibbon RT *et al*. 2015 MDTraj: a modern open library for the analysis of molecular dynamics trajectories. *Biophys. J*. **109**, 1528–1532. (doi:10.1016/j.bpj.2015.08.015)
35. Grant BJ, Rodrigues APC, ElSawy KM, McCammon JA, Caves LSD. 2006 Bio3d: an R package for the comparative analysis of protein structures. *Bioinformatics* **22**, 2695–2696. (doi:10.1093/bioinformatics/btl461)
36. Humphrey W, Dalke A, Schulten K. 1996 VMD: visual molecular dynamics. *J. Mol. Graph.* **14**, 33–38. (doi:10.1016/0263-7855(96)00018-5)
37. Miller BR, McGee TD, Swails JM, Homeyer N, Gohlke H, Roitberg AE. 2012 MMPBSA.py: an efficient program for end-state free energy calculations. *J. Chem. Theory Comput*. **8**, 3314–3321. (doi:10.1021/ct300418h)
38. Valdés-Tresanco MS, Valdés-Tresanco ME, Valiente PA, Moreno E. 2021 gmx_MMPBSA: a new tool to perform end-state free energy calculations with GROMACS. *J. Chem. Theory Comput*. **17**, 6281–6291. (doi:10.1021/acs.jctc.1c00645)
39. Zhu Y, Rahman T. Conformational footprints of Agonism: Differences of Inositol 1,4,5-trisphosphate (IP_3) and Adenophostin a on IP_3 receptor's n-terminal dynamics [Dataset]. Dryad Digital Repository. (doi:10.5061/dryad.98sf7m0wp)
40. Zhu Y, Rahman T. 2026 Supplementary material from: Conformational Footprints of Agonism: Differences of Inositol 1,4,5-trisphosphate (IP_3) and Adenophostin A on IP_3 Receptor's N-Terminal Dynamics. Figshare. (doi:10.6084/m9.figshare.c.8249996)